# Hyperbolic Plasmons in Coupled Luttinger Liquids of Homochiral Carbon Nanotube Arrays

Saiqun Ma(马赛群)[1,2†], Jiajun Chen(陈佳俊)[1,2†], Cheng Hu(胡成)[1,2], Kunqi Xu(徐琨淇)[1,2], Yufeng Xie(谢宇烽)[1,2], Xingdong Luo(骆兴东)[1,2], Zhenghan Wu(吴正瀚)[1,2], Yi Chen(陈一)[1,2], Xianliang Zhou(周先亮)[1,2], Shuo Lou(娄硕)[1,2], Bosai Lyu(吕博赛)[1,2], Peiyue Shen(沈沛约)[1,2], Zhichun Zhang(张智淳)[1,2], Aolin Deng(邓奥林)[1,2], Chengjia Zhang(张诚嘉)[1,2], Qi Liang(梁齐)[1,2,3], Ming Tian(田明)[4], Neng Wan(万能)[4], Ji-Hun Kang[5,6], and Zhiwen Shi(史志文)[1,2,3*]

[1]*Key Laboratory of Artificial Structures and Quantum Control (Ministry of Education), School of Physics and Astronomy, Shanghai Jiao Tong University, Shanghai 200240, China*
[2]*Collaborative Innovation Centre of Advanced Microstructures, Nanjing University, Nanjing 210093, China*
[3]*Tsung-Dao Lee Institute, Shanghai Jiao Tong University, Shanghai 200240, China*
[4]*Key laboratory of MEMS of Ministry of Education, School of Integrated Circuits, Southeast University, Nanjing 210096, China*
[5]*Department of Optical Engineering, Kongju National University, Cheonan 31080, Korea*
[6]*Department of Future Convergence Engineering, Kongju National University, Cheonan 31080, Korea*

(Received 4 June 2025; accepted manuscript online 1 August 2025)

A Luttinger liquid is a theoretical model describing interacting electrons in one-dimensional (1D) conductors. While individual 1D conductors have shown interesting Luttinger-liquid behaviors such as spin–charge separation and power-law spectral density, the more interesting phenomena predicted in coupled Luttinger liquids of neighboring 1D conductors have been rarely observed due to the difficulty in creating such structures. Recently, we have successfully grown close-packed carbon nanotube (CNT) arrays with uniform chirality, providing an ideal material system for studying the coupled Luttinger liquids. Here, we report on the observation of tunable hyperbolic plasmons in the coupled Luttinger liquids of CNT arrays using scanning near-field optical microscopy. These hyperbolic plasmons, resulting from the conductivity anisotropy in the CNT array, exhibit strong spatial confinement, *in situ* tunability, and a wide spectral range. Despite their hyperbolic wavefronts, the plasmon propagation in the axial direction still adheres to the Luttinger-liquid theory. Our work not only demonstrates a fascinating phenomenon in coupled Luttinger liquids for fundamental physics exploration, but also provides a highly confined and *in situ* tunable hyperbolic plasmon in close-packed CNT arrays for future nanophotonic devices and circuits.

DOI: 10.1088/0256-307X/42/9/090710 CSTR: 32039.14.0256-307X.42.9.090710

The dielectric permittivity of a material determines its electromagnetic response. If a material is highly anisotropic, with metallic conductivity in one direction and insulating in another, different components of its dielectric permittivity tensor may have opposite signs. This leads to a hyperbolic dispersion equation governing light propagation within these materials, which are known as "hyperbolic materials".[1,2] These unique materials have attracted significant attention for their ability to manipulate electromagnetic waves and control light propagation, showcasing properties not commonly seen in regular materials. Previous studies have highlighted features, such as negative refraction,[3–5] hyperlens,[6] and enhanced spontaneous emission,[7] indicating their potential for application in advanced optical devices. Recent studies have reported hyperbolic phonon polaritons in natural hyperbolic materials such as hexagonal boron nitride (hBN)[8–12] and molybdenum trioxide ($MoO_3$).[13–16] However, the spectral range of these hyperbolic phonon polaritons is rather narrow, which has strongly hindered their practical applications. On the contrary, plasmon polaritons typically possess a much broader spectral range, thus are highly desirable. Up to now, experimental imaging of hyperbolic plasmon polaritons remains scarce, with their presence only confirmed in graphene/$MoO_3$ hybrid system[4] and in $MoOCl_2$,[17,18] despite numerous studies on the hyperbolic phonon polaritons.[8,14–16,19–22]

On the other hand, close-packed carbon nanotube (CNT) arrays with strong anisotropy provide possibility for studying the hyperbolic plasmons. Individual CNTs are the best-known one-dimensional (1D) materials with electrons behaving as a Luttinger liquid,[23–25] and closely

†These authors contributed equally to this work.
*Corresponding author. Email: zwshi@sjtu.edu.cn
© 2025 Chinese Physical Society and IOP Publishing Ltd. All rights, including for text and data mining, AI training, and similar technologies, are reserved.

packed arrays of CNTs are considered as "coupled Luttinger liquids".[26] It has been predicted that such a system possesses a two-dimensional (2D) anisotropic non-Fermi-liquid phase,[27] showing Luttinger-liquid-like behavior along the nanotubes but insulating characteristics across them. This anisotropic property endows CNT arrays with hyperbolic plasmons. Theoretical analyses and spectral studies have offered compelling proof of hyperbolic properties in CNT arrays.[28–32] Lately, we have successfully grown arrays of close-packed, well-aligned CNTs with uniform chirality, creating an ideal setting for exploring hyperbolic plasmons.

In this study, we report on the observation of hyperbolic plasmons in coupled Luttinger liquids of CNT arrays using scanning near-field optical microscopy (SNOM). The observed hyperbolic plasmons exhibit strong spatial confinement and high tunability, indicating their potential for application in advanced optical devices. These appealing features are well captured by the effective medium numerical simulations and the Luttinger-liquid theory. We further demonstrated manipulation of the hyperbolic plasmons through *in situ* cutting of the CNT arrays using electrode-free anodic oxidation nanolithography.[33] Our study marks the first observation of strongly confined hyperbolic plasmons in the coupled Luttinger liquids, opening up possibilities for their application in future advanced nanophotonic devices and for further exploration of intriguing phenomena in coupled Luttinger-liquids.

To quantitatively analyze the hyperbolic electromagnetic response of CNT arrays, we model them as an anisotropic medium. A diagram in Fig. 1(a) illustrates the arrangement of close-packed, parallel metallic CNTs within an array. This structure is electrically conductive along the CNTs and largely insulating across them.[27] Since the diameter of the nanotubes is much smaller than the wavelength of either the excitation infrared light or the generated plasmons, the nanotube array can be treated as a flat plate with anisotropic conductivity based on the effective medium theory,[29,32,34] as illustrated in Fig. 1(b). The low-frequency optical conductivity used in our model is determined through a bulk equivalent approach.[34] Detailed calculation of the conductivity can be found in the *Methods* section.

Subsequently, we utilized the finite element method (COMSOL Multiphysics) to simulate the distribution of the electromagnetic field of plasmons in the CNT array. Details of the simulation process can be found in the *Methods* section. By placing an electric dipole exciter at the center of the effective anisotropic medium, we successfully captured the distribution of the electric field of the excited plasmon polaritons. Unlike plasmons in an isotropic medium with typically convex or circular wavefronts propagating isotropically, distinct concave-shaped wavefronts propagating along the horizontal direction are visible, as depicted in Fig. 1(c). The Fourier transform of the concave wavefronts is shown in Fig. 1(d), where the black dashed lines represent a fitted hyperbolic iso-frequency contour. Our simulation unambiguously demonstrates that the highly anisotropic medium of CNT arrays supports hyperbolic plasmon modes.

To experimentally observe the hyperbolic plasmons, CNT arrays were first grown using the catalytic chemical vapor deposition method,[35] details of which can be found in the *Methods* section. Figure 2 presents characterizations of two representative CNT arrays, including both topographical and spectral features. In Fig. 2(a), a large-scale atomic force microscopy (AFM) topography image shows an as-grown CNT array on a hBN substrate.

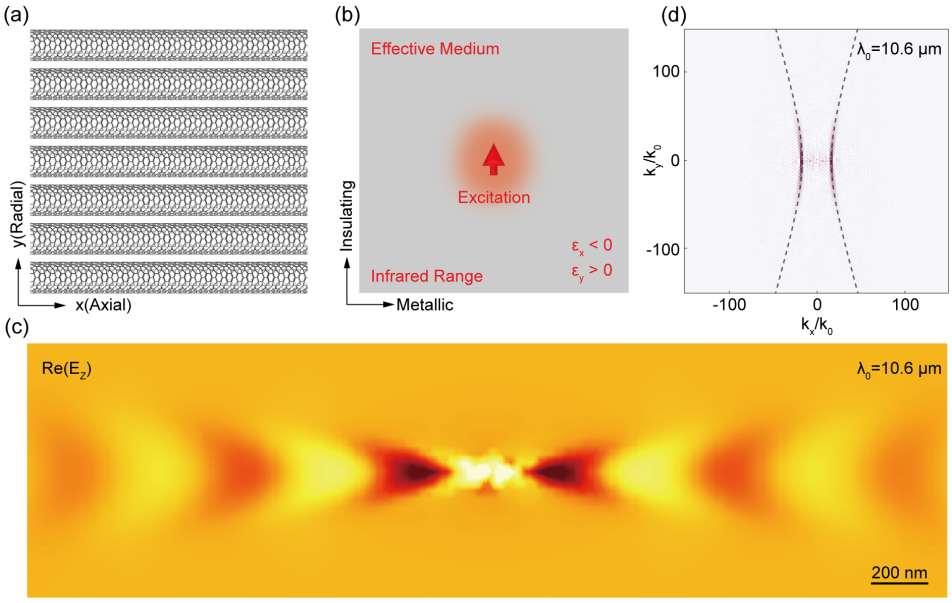


**Fig. 1.** Numerical simulation of hyperbolic plasmons in highly anisotropic medium of CNT arrays. (a) A schematic of the structure of a close-packed parallel CNT array. (b) Equivalent anisotropic medium of the CNT array with one direction metallic and the other direction insulating. The red arrow represents the dipole used to excite plasmons in our numerical simulations. (c) Simulated distribution of the real part of the plasmon field Re($E_z$), taken right above CNT array. (d) Fourier transform of the plasmon field in (c), showing a hyperbolic iso-frequency contour.

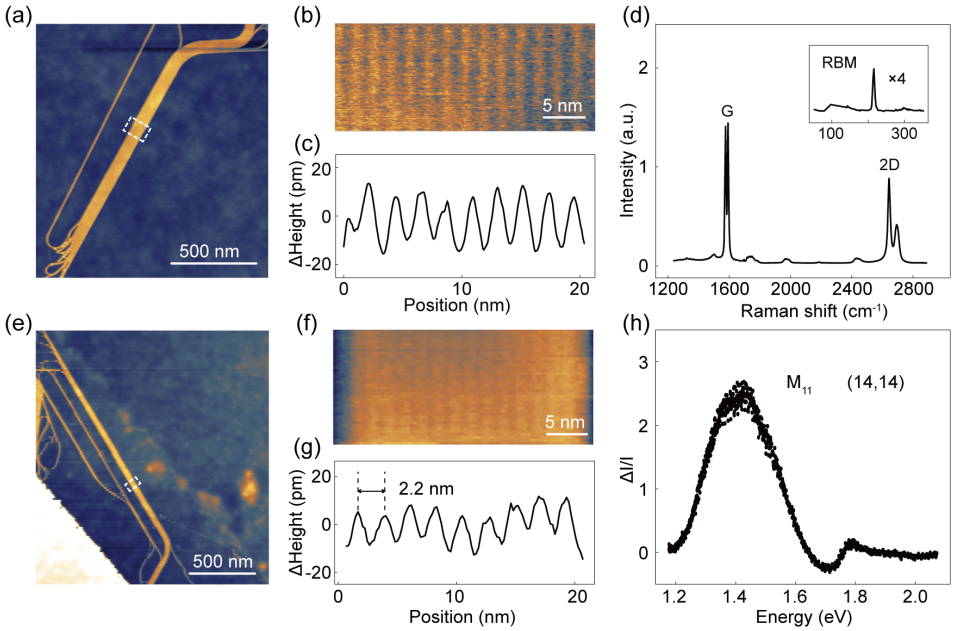


**Fig. 2.** Characterizations of representative CNT arrays with uniform chirality. (a) AFM topography of a CNT array on hBN. Scale bar: 500 nm. (b) A zoom-in image of the CNT array (indicated by the dashed square area) in (a), showcasing close-packed individual CNTs. Scale bar: 5 nm. (c) Cross-sectional lineprofile of the array in (b). (d) Raman spectrum of the CNT array in (a), with the G mode, 2D mode, and RBM mode marked. The single RBM-mode peak indicates that all the CNTs have the same chirality. (e)–(g) Topography characterization of another CNT array. The period of 2.2 nm corresponds to the sum of the CNT diameter and the inter-tube wall-to-wall vdW distance of 0.3 nm. (h) Rayleigh spectrum of the CNT array in (e) shows a scattering peak at 1.44 eV, from which a chirality of (14, 14) can be obtained.

The ultra-flat hBN substrate and the low-noise AFM technique allowed for the identification of individual nanotubes within the array. These CNTs exhibit well alignment and parallelism, as evidenced by the magnified view presented in Fig. 2(b) and the cross-sectional line profile displayed in Fig. 2(c). Additional characterizations of another CNT array are presented in Figs. 2(e)–2(g). Beyond these topographical analyses, figures 2(d) and 2(h) display the Raman and Rayleigh spectra, respectively. The Raman spectrum reveals prominent signals corresponding to the G mode, 2D mode, and radial breathing mode (RBM) of the CNT arrays. The Raman RBM signal exhibits a single peak, indicating the uniform chirality within the array. The chirality of the CNTs can be further determined through Rayleigh spectroscopy,[36] which probes the CNT inter-band optical transitions. As depicted in Fig. 2(h), the presence of a single, dominant scattering peak centered at 1.44 eV indicates that all the nanotubes within the entire CNT array exhibit uniform chirality with indices of (14, 14), suggesting that CNTs are metallic with a diameter of 1.9 nm. Considering a van der Waals (vdW) spacing of ∼0.3 nm between adjacent CNTs,[31] stacking these CNTs together will generate a periodic pattern of 2.2 nm, which agrees well with the AFM measurement [Fig. 2(g)]. Characterization of many other CNT arrays with varying widths can be found in Fig. S2 of the supplementary materials (SM), which consistently demonstrates the high quality and uniformity of the as-grown CNT arrays, making them an ideal platform for studying hyperbolic plasmons.

Next, to experimentally investigate hyperbolic plasmons in the as-grown CNT arrays, we employed the SNOM technique, as illustrated in Fig. 3(a). In this technique, infrared light was focused onto the apex of a metallic AFM tip with a radius of approximately 10 nm. The tip acted as a point excitation source, effectively exciting plasmon waves within the CNT arrays. The excited plasmon waves propagated in the CNT arrays and were reflected back at the CNT terminals, causing interference with the local field underneath the tip. This interference consequently modified the intensity of the tip-scattering, which was detected by an HgCdTe detector in the far field. When capturing the plasmon interference patterns, a sharp boundary was typically required to reflect plasmons with well-defined phase. It is important to note that the CNT array usually does not have a sharp terminal, as displayed in Figs. 2(a) and 2(e). Therefore, to create regular and sharp terminals, an additional AFM cutting process using the electrode-free anodic oxidation nanolithography technique[33] was commonly conducted prior to the near-field optical imaging. For more detailed information on the cutting process, please refer to Section 3 of the SM. These created terminals can reflect plasmons with a well-defined phase, thus helping the observation of plasmons in the CNT array.

Near-field optical images of plasmons in six arrays of varying widths are presented in Fig. 3(b). As the number of CNTs within each array increases from 1 (the top panel) to ∼85 (the bottom panel), the plasmon wavelength of the arrays also increases in a systematic manner. Notably, a distinct concave-shaped plasmon wavefront pattern emerges in relatively wider arrays shown in the

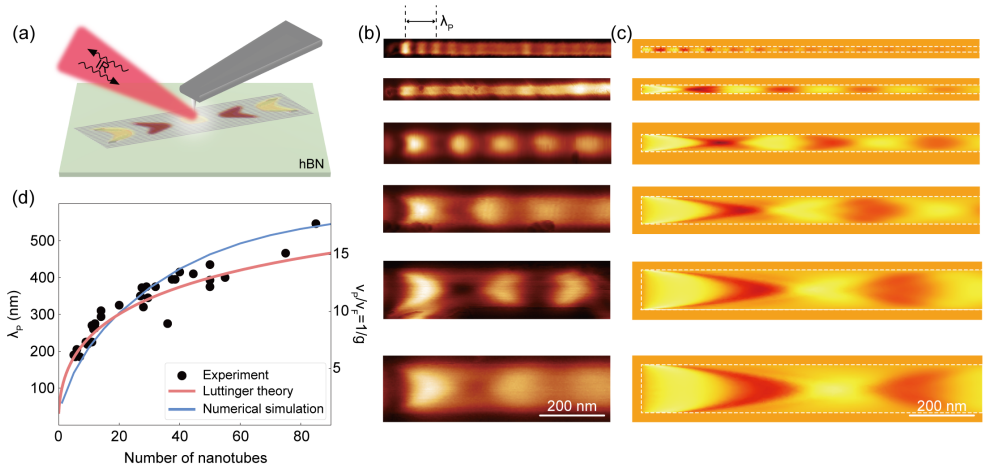


**Fig. 3.** Experimental observation of hyperbolic Luttinger-liquid plasmons in CNT arrays. (a) Schematic of excitation and imaging of plasmons in a CNT array using SNOM. (b) Near-field IR images of plasmons in CNT arrays of different widths. From top to bottom, the arrays contain 1, 6, ∼36, ∼50, ∼75, ∼85 CNTs. Scale bar: 200 nm. (c) Simulated plasmon fields in CNT arrays of varying widths. The white dashed lines mark the boundaries of CNT arrays. The topmost image has been vertically stretched for better visibility. (d) Plasmon wavelengths plotted for arrays of varying number of CNTs. Results obtained from numerical simulation, Luttinger theory, and experiments show good agreement.

bottom three panels. This is in stark contrast to the 1D plasmons with a point wavefront in individual CNTs. The concave pattern is a characteristic feature of the hyperbolic polaritons, which is also observed in plasmons of other hyperbolic materials.[13,15,22] We performed simulations of plasmons in arrays with different numbers of CNTs, the results of which are shown in Fig. 3(c), illustrating that the hyperbolic wavefront becomes more prominent as the number of CNTs increases. Further detailed analysis of the concave-shaped wavefront can be found in Section 5 of the SM.

Notably, the plasmon wavelength along the tube axis direction can still be described by the Luttinger-liquid theory with a single parameter $g$. Note that we have assumed that the inter-tube coupling is purely capacitive coupling with no inter-tube electron tunneling. In the Luttinger-liquid theory, individual metallic CNTs possess plasmons with velocity $v_\mathrm{p}$ and wavelength $\lambda_\mathrm{p} = \frac{v_\mathrm{p}}{c}\lambda_0$ determined by the relationship[24,37] $\frac{1}{g} = \frac{v_\mathrm{p}}{v_\mathrm{F}} \approx \sqrt{1 + e^2 \frac{8}{\varepsilon_\mathrm{eff}\pi\hbar v_\mathrm{F}} \ln(\frac{R_\mathrm{s}}{R})}$, where $v_\mathrm{F}$ is the Fermi velocity, $R$ is the radius of CNTs, $\varepsilon_\mathrm{eff}$ is the effective dielectric constant due to substrate screening, and $R_\mathrm{s} = \frac{\lambda_\mathrm{p}}{2\pi}$ is the effective screening length. This relationship is derived from a concentric metal shell model for an individual single-walled CNT, and agrees quantitatively well with experimental observations.[24,38] When considering plasmons in the CNT arrays, we have developed a concentric elliptical capacitor model based on the planar array structure. Consequently, the aforementioned relationship undergoes modification to accommodate the array characteristics,

$$\frac{1}{g} = \frac{v_\mathrm{p}}{v_\mathrm{F}} \approx \sqrt{1 + e^2 \frac{8N}{\varepsilon_\mathrm{eff}\pi\hbar v_\mathrm{F}} \ln\left[\frac{(N-1)(2R+d)+\pi R_\mathrm{s}}{(N-1)(2R+d)+\pi R}\right]},$$

where $N$ is the number of CNTs in the array, $d$ is the vdW distance between adjacent CNTs. The derivation of this modified relationship can be found in Section 1 of the SM. Based on this modified relationship, we have obtained the plasmon wavelength as a function of the number of CNTs, as plotted in Fig. 3(d). Within the same panel, we also present the experimentally extracted plasmon wavelengths, along with the numerical simulation results, which agree quite well with each other. It is worth noting that the Luttinger-liquid parameter $g$, which describes the type and strength of the interaction, can also be determined. Basically, non-interacting electron gases correspond to a value of $g = 1$, while attractive interactions exhibit $g > 1$ and repulsive interactions have $g < 1$. Changes in plasmon wavelength alter the Luttinger-liquid parameter $g$, suggesting potential enhancements in electron–electron interactions within the nanotube arrays. This opens up possibilities for uncovering new correlation phenomena in the nanotube arrays in future research.

To further explore the hyperbolic characteristics of the plasmons in CNT arrays, we intentionally created slanted boundaries at the ends of a CNT array and investigated the resulting plasmon interference patterns. Figure 4(a) shows a near-field optical image of a CNT array with a vertical terminal on the left and a tilted terminal on the right, revealing distinct plasmonic patterns between the two terminals. The vertical terminal on the left forms a concave-shaped pattern, while the 60-degree slanted boundary on the right forms an oblique-linear plasmon propagating in the opposite direction, as marked by the green arrows. The formation of the oblique-linear plasmon pattern on the slanted boundary involves a complex process. Firstly, such a slanted boundary coherently reflects plasmon wavefronts in a specific direction [red lines in Fig. 4(b)], and leads to a selection of a 60-degree wavevector $\boldsymbol{k}(60°)$ and a corresponding Poynting vector $\boldsymbol{S}$, which are depicted on a hyperbolic iso-frequency curve in Fig. 4(e). This is similar to the edge-tailored phonon polaritons[13]

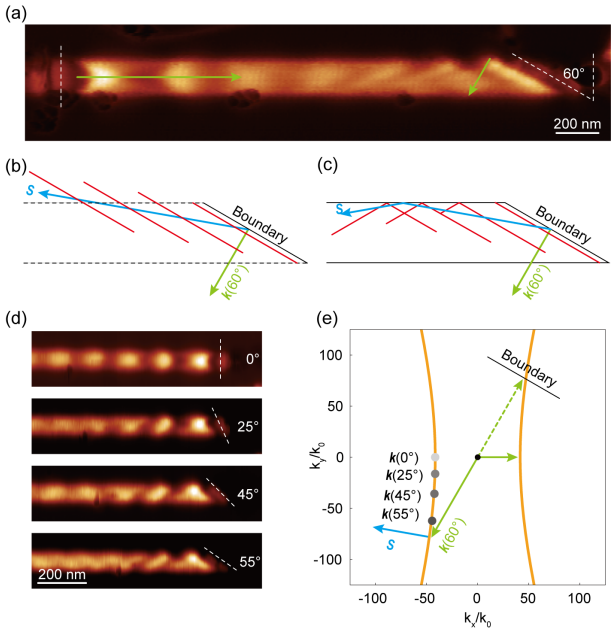


**Fig. 4.** Tailoring hyperbolic plasmons with tilted boundaries. (a) A near-field IR image of two different boundary-tailored plasmon modes within one CNT array. Scale bar: 200 nm. (b) Tailored plasmon wave by a 60-degree boundary. The wave vector $\boldsymbol{k}$ is marked by the green vector, the Poynting vector $\boldsymbol{S}$ is marked by the blue vector, and the red lines denote the plasmon wavefront. (c) Boundary-tailored plasmon wave and its reflection by a boundary along the nanotube direction. (d) Tailored plasmon modes by four boundaries with different tilting angles. White dashed lines outline the tilted boundaries of CNT arrays. Scale bar: 200 nm. (e) Boundary angle dependent selection of wavevector $\boldsymbol{k}$ of the hyperbolic plasmons shown in the iso-frequency contour. $\boldsymbol{k}(60°)$ corresponds to the wavevector of plasmon mode displayed in (a). $\boldsymbol{k}(0°)$, $\boldsymbol{k}(25°)$, $\boldsymbol{k}(45°)$, and $\boldsymbol{k}(55°)$ correspond to wavevectors of plasmon modes shown in (d).

observed in 2D hyperbolic material of $\alpha$-$MoO_3$. Then, side boundaries of the CNT arrays will further reflect plasmons, resulting in a plasmon interference pattern shown in Fig. 4(c). This explains the experimentally observed plasmon patterns near the slanted terminal of the CNT array in Fig. 4(a). Notably, the oblique-linear plasmon wavelength at the right terminal is only about half of the plasmon wavelength at the left terminal. Correspondingly, the magnitude of the oblique wavevector $\boldsymbol{k}(60°)$ is larger than the horizontal $\boldsymbol{k}$ vector [Fig. 4(e)], representing stronger spatial confinement.

Furthermore, we demonstrate the unique capability to selectively choose plasmon modes by altering the tilting angles of terminal boundaries in a CNT array. As shown in Fig. 4(d), by adjusting the boundary angle four times, starting from 0° to 25°, 45°, and 55°, we observed a gradual change in the plasmon interference pattern from concave to oblique-linear, with corresponding $\boldsymbol{k}$ wavevectors marked in Fig. 4(e). The ability to manipulate plasmon modes in CNT arrays presents a significant advantage over isotropic materials like graphene. Considering their broad spectral range and low loss, CNT arrays hold great potential for *in situ* manipulation of plasmon modes in nanoscale plasmonic devices.

Notably, the hyperbolic plasmons in CNT arrays exhibit remarkable spatial confinement. The plasmon wavelengths at both vertical and oblique boundaries are significantly smaller than the excitation wavelength, with the oblique boundary achieving a wavelength confinement factor over 100 times. The theoretical confinement for plasmons in CNT arrays can be even larger, as the magnitude of the wavevector $\boldsymbol{k}$ in a hyperbolic dispersion is unlimited. Fortunately, CNT array structures are extremely compact, with a thickness (equivalent to the diameter of a single CNT) and a unit cell width (equivalent to the diameter of a single CNT plus the vdW distance) of a few nanometers. The ultra-small size of the CNT arrays allows for a larger theoretical upper limit of the wavevector, given by $k_{\max} \sim 1/a$, offering significant potential for device miniaturization. Additionally, the CNT arrays are readily accessible and can be tailored for specific needs, making them highly convenient for plasmonic device fabrication.

In addition to being a fantastic hyperbolic material, CNT arrays also provide a platform for studying correlated physics. The axial plasmon wavelength varies with the number of CNTs, reflecting changes in the Luttinger-liquid parameter $g$ and in electron–electron interaction. More importantly, the CNT array serves as an ideal platform for demonstrating novel physics that has long been investigated in the theoretical "coupled wire model", a setup that has received extensive theoretical study [26,39,40] but has rarely been realized experimentally. [41] The observation of hyperbolic plasmons within CNT arrays represents the first direct realization of this model, confirming the existence of a distinctive "coupled Luttinger-liquid" phase. [27] Thanks to the rich structures of individual CNTs, the array can be further customized by adjusting CNT chirality, spacing, and the number of CNTs. This provides a considerable degree of freedom to manipulate electron–electron interactions and conduct further studies of correlated physics in the 1D to 2D crossover.

To conclude, we have observed strongly confined hyperbolic plasmons in coupled Luttinger liquids constructed by arrays of homochiral single-walled CNTs. The hyperbolic plasmons originate from the strong anisotropy in optical conductivity along and across the nanotube axial direction. Despite exhibiting hyperbolic wavefronts, the plasmons still follow the Luttinger-liquid theory when propagating along the axial direction. Our study has focused on elucidating the propagation and manipulation of the hyperbolic plasmons, as well as exploring their Luttinger-liquid behaviors. The hyperbolic Luttinger-liquid plasmons are highly compact and easily tailored, making them promising candidates for plasmonic and nanophotonic devices. Furthermore, our study has deepened the understanding of the strong anisotropic coupled Luttinger-liquid system. Future explorations involving the application of magnetic fields are anticipated to uncover novel topological phases and additional intriguing interaction phenomena. [42,43]

*Methods.*

*Effective Medium Theory for the CNT Arrays.* The conductivity of CNT arrays can be achieved by following

a previously reported process.[34,44] First, the axial complex surface conductivity of an individual metallic zigzag CNT with a chirality of $(m,\ 0)$ at frequencies below the first inter-band transition is

$$\sigma_{\mathrm{CNT}}(\omega) \cong \mathrm{i}\frac{2\sqrt{3}e^2\gamma_0}{m\pi\hbar^2(\omega+\mathrm{i}\nu)},$$

where $e$ is the electron charge, $\gamma_0 = 2.7\,\mathrm{eV}$ is the overlapping integral,[45] $\nu$ is the relaxation frequency and $\hbar$ is the reduced Plank's constant.

The surface conductivity needs to be transformed into bulk conductivity for application in numerical simulations. We then treat a CNT and the air inside it as a nanowire (NW) and convert the conductivity of the CNT to that of the NW. Consider the electrical field over the cross-section, as the distributed Ohm's law

$$I(z,\omega) = \frac{E_z(z,\omega)}{Z(z,\omega)},$$

where $I(z,\omega)$ is the net current across the CNT cross-section at $z$, $E_z(z,\omega)$ is the electrical field component along $z$ in the CNT at $z$ and $Z(z,\omega)$ is its distributed impedance. For an equivalent NW, we have

$$Z_{\mathrm{NW,bulk}}(z,\omega) = Z_{\mathrm{CNT,surf}}(z,\omega).$$

So,

$$\iint_{\text{cross section}} \sigma_{\mathrm{NW}}(z,\omega)\mathrm{d}A = \int_{\text{perimeter}} \sigma_{\mathrm{CNT}}(z,\omega)\mathrm{d}l,$$

where $\sigma_{\mathrm{NW}}(z,\omega)$ is the bulk conductivity of the equivalent NW and $\sigma_{\mathrm{CNT}}(z,\omega)$ is the surface conductivity of the original CNT. Therefore, we have

$$\sigma_{\mathrm{NW}}(z,\omega) = \sigma_{\mathrm{CNT}}(z,\omega)\frac{P_{\mathrm{CNT}}}{\Phi_{\mathrm{CNT}}},$$

where $P_{\mathrm{CNT}}$ is the perimeter of CNT and $\Phi_{\mathrm{CNT}}$ is the area of the cross-section of the CNT.

Considering an array of NWs (equivalent to the CNT array), the volume fraction of NWs $\delta_{\mathrm{NW}}$ is equal to the proportion of cross-sectional area occupied by the NWs, that is,

$$\delta_{\mathrm{NW}} = \frac{N_{\mathrm{NW}}\Phi_{\mathrm{NW}}}{\Phi_{\mathrm{array}}} = \Phi_{\mathrm{NW}}D_{\mathrm{NW}},$$

where $\Phi_{\mathrm{array}}$ is the cross-sectional area of the array, $\Phi_{\mathrm{NW}}$ is the cross-sectional area of one NW, $N_{\mathrm{NW}}$ is the number of NW in this array, and $D_{\mathrm{NW}}$ is the density of NW (number of NW per unit area). So, the effective axial conductivity $\sigma_{\mathrm{axial}}$ is the average value of the conductivity of NWs and the air ($\sigma_{\mathrm{air}} = 0$), that is,

$$\sigma_{\mathrm{array}} = \sigma_{\mathrm{NW}}\delta_{\mathrm{NW}} = \sigma_{\mathrm{CNT}}P_{\mathrm{CNT}}D_{\mathrm{CNT}},$$

where $P$ is the perimeter of CNTs and $D$ is the density of CNTs (number of CNTs per unit area). Finally, by introducing the parameters of the CNT arrays in our experiment, we can obtain the conductivity. The axial bulk conductivity of an array of CNTs with chirality index of (21, 0) is calculated to be $(756 + 4.03\times10^5\mathrm{i})\,\mathrm{S/m}$. CNTs with such chirality have a diameter of ∼1.5 nm, a typical value for our CNT samples.

For the radial conductivity, it is difficult to determine the precise values. Given that the radial direction is charge insulating in coupled Luttinger-liquid,[27] we simplify the radial conductivity to that of the air, similar treatments have also been reported in previous research on CNT arrays.[30,32,34]

A more rigorous effective medium theory requires effective descriptions of both permittivity (or conductivity) and permeability, which can be achieved using the Maxwell–Garnett theory or the Bruggeman approximation.[46,47]

*Growth of CNT Arrays.* First, hBN flakes were mechanically exfoliated onto $SiO_2$/Si substrates, followed by exposure to hydrogen plasma at 300 ℃ to remove all organic residuals. Then, a 0.05 nm-thick Fe film was deposited on the hBN-covered $SiO_2$/Si surfaces through thermal evaporation (evaporation rate: ∼0.005 nm/s, base vacuum pressure: $\sim1\times10^{-6}$ mbar), serving as catalytic nanoparticles for the CNT growth. After that, the chips were placed into a 1-inch-diameter quartz tube furnace (Anhui BEQ Equipment Technology) and gradually heated to the growth temperature (800–850 ℃) under hydrogen and argon gases at atmospheric pressure. When the growth temperature was reached, argon was replaced by methane to initiate the CNT growth. After a typical growth duration of 60 minutes, the system was cooled down to room temperature under a protective atmosphere of hydrogen and argon.

*Infrared Nano-Imaging and High-Resolution AFM.* Our home-made scattering-type SNOM setup was based on a commercial AFM (Bruker Innova). A beam of $CO_2$ laser with a 10.6 μm wavelength was illuminated onto a gold-coated AFM tip (HQ-NSC35/Cr-Au), creating a near-field hot spot at the tip apex. To capture the infrared radiation scattered by the tip, an HgCdTe detector was positioned in the far field. In order to suppress background scattering from the cantilever and the sample, the tip was vibrated vertically with an amplitude of ∼50 nm at a frequency of about 200 kHz, and the detector signal was demodulated at a higher-order harmonic frequency by a lock-in amplifier (Zurich Instruments, HF2LI). The high-resolution topographical images presented in the main text and the SM, which illustrate the number of CNTs within an array, were recorded by a commercial AFM (Cypher S, Oxford Instruments). These images were captured in AC mode (tapping mode) under ambient conditions, using AFM probes of the RTESPA-300 type.

*COMSOL Simulation.* Numerical simulations were conducted using the wave optics module of the commercial software package COMSOL. The focus was solely on the electric field component normal to the sample surface ($E_z$). The mesh size was set to "refined". The excitation light frequency was set to 28.28 THz to match the experimental 10.6 μm wavelength. In the simulation shown in Fig. 1, an electrical dipole was placed 50 nm above a $4\times10\,\mu\mathrm{m}^2$ plane. The real part of the $E_z$ component [$\mathrm{Re}(E_z)$] was recorded on the plane surface. For the simulations shown in Fig. 3 and Fig. S5 of the SM, a beam of light polarized

perpendicular to the vertical boundary was irradiated onto the surface of the plane to excite plasmons. The excited plasmons were recorded at the plane surface.

*Acknowledgements.* This work was supported by the National Key R&D Program of China (Grant No. 2021YFA1202902), and the National Natural Science Foundation of China (Grant Nos. 12374292 and 12074244). B.L. acknowledges support from the Development Scholarship for Outstanding Ph.D. of Shanghai Jiao Tong University. J.K. acknowledges support from the National Research Foundation of Korea (NRF) grant funded by the Korean government (MSIT) (Grant No. NRF-RS-2024-00454528).

## References

[1] Ferrari L, Wu C, Lepage D, Zhang X, and Liu Z 2015 *Prog. Quantum Electron.* **40** 1
[2] Poddubny A, Iorsh I, Belov P, and Kivshar Y 2013 *Nat. Photon.* **7** 948
[3] High A A, Devlin R C, Dibos A, Polking M, Wild D S, Perczel J, de Leon N P, Lukin M D, and Park H 2015 *Nature* **522** 192
[4] Hu H, Chen N, Teng H, Yu R, Xue M, Chen K, Xiao Y, Qu Y, Hu D, Chen J, Sun Z, Li P, de Abajo F J G, and Dai Q 2023 *Science* **379** 558
[5] Sternbach A J, Moore S L, Rikhter A, Zhang S, Jing R, Shao Y, Kim B S Y, Xu S, Liu S, Edgar J H, Rubio A, Dean C, Hone J, Fogler M M, and Basov D N 2023 *Science* **379** 555
[6] Casse B D F, Lu W T, Huang Y J, Gultepe E, Menon L, and Sridhar S 2010 *Appl. Phys. Lett.* **96** 023114
[7] Lu D, Kan J J, Fullerton E E, and Liu Z 2014 *Nat. Nanotech.* **9** 48
[8] Dai S, Fei Z, Ma Q, Rodin A S, Wagner M, McLeod A S, Liu M K, Gannett W, Regan W, Watanabe K, Taniguchi T, Thiemens M, Dominguez G, Neto A H C, Zettl A, Keilmann F, Jarillo-Herrero P, Fogler M M, and Basov D N 2014 *Science* **343** 1125
[9] Shi Z W, Bechtel H A, Berweger S, Sun Y H, Zeng B, Jin C H, Chang H, Martin M C, Raschke M B, and Wang F 2015 *ACS Photonics* **2** 790
[10] Giles A J, Dai S, Glembocki O J, Kretinin A V, Sun Z, Ellis C T, Tischler J G, Taniguchi T, Watanabe K, Fogler M M, Novoselov K S, Basov D N, and Caldwell J D 2016 *Nano Lett.* **16** 3858
[11] Duan J, Chen R, Li J, Jin K, Sun Z, and Chen J 2017 *Adv. Mater.* **29** 1702494
[12] Yoxall E, Schnell M, Nikitin A Y, Txoperena O, Woessner A, Lundeberg M B, Casanova F, Hueso L E, Koppens F H L, and Hillenbrand R 2015 *Nat. Photon.* **9** 674
[13] Dai Z, Hu G, Si G, Ou Q, Zhang Q, Balendhran S, Rahman F, Zhang B Y, Ou J Z, Li G, Alù A, Qiu C W, and Bao Q 2020 *Nat. Commun.* **11** 6086
[14] Zheng Z B, Chen J N, Wang Y, Wang X M, Chen X B, Liu P Y, Xu J B, Xie W G, Chen H J, Deng S Z, and Xu N S 2018 *Adv. Mater.* **30** e1705318
[15] Zheng Z B, Xu N S, Oscurato S L, Tamagnone M, Sun F S, Jiang Y Z, Ke Y L, Chen J N, Huang W C, Wilson W L, Ambrosio A, Deng S Z, and Chen H J 2019 *Sci. Adv.* **5** eaav8690
[16] Ma W, Alonso-Gonzalez P, Li S, Nikitin A Y, Yuan J, Martin-Sanchez J, Taboada-Gutierrez J, Amenabar I, Li P, Velez S, Tollan C, Dai Z, Zhang Y, Sriram S, Kalantar-Zadeh K, Lee S T, Hillenbrand R, and Bao Q 2018 *Nature* **562** 557
[17] Ruta F L, Shao Y, Acharya S, Mu A, Jo N H, Ryu S H, Balatsky D, Pashov D, Kim B S Y, Katsnelson M I, Analytis J G, Rotenberg E, Millis A J, van Schilfgaarde M, and Basov D N 2024 arXiv:2406.05703 [cond-mat.str-el]
[18] Venturi G, Mancini A, Melchioni N, Chiodini S, and Ambrosio A 2024 *Nat. Commun.* **15** 9727
[19] Caldwell J D, Kretinin A V, Chen Y, Giannini V, Fogler M M, Francescato Y, Ellis C T, Tischler J G, Woods C R, Giles A J, Hong M, Watanabe K, Taniguchi T, Maier S A, and Novoselov K S 2014 *Nat. Commun.* **5** 5221
[20] van Veen E, Nemilentsau A, Kumar A, Roldán R, Katsnelson M I, Low T, and Yuan S 2019 *Phys. Rev. Appl.* **12** 014011
[21] Low T, Roldán R, Wang H, Xia F, Avouris P, Moreno L M, and Guinea F 2014 *Phys. Rev. Lett.* **113** 106802
[22] Li P N, Dolado I, Alfaro-Mozaz F J, Casanova F, Hueso L E, Liu S, Edgar J H, Nikitin A Y, Vélez S, and Hillenbrand R 2018 *Science* **359** 892
[23] Bockrath M, Cobden D H, Lu J, Rinzler A G, Smalley R E, Balents L, and McEuen P L 1999 *Nature* **397** 598
[24] Shi Z W, Hong X P, Bechtel H A, Zeng B, Martin M C, Watanabe K, Taniguchi T, Shen Y R, and Wang F 2015 *Nat. Photon.* **9** 515
[25] Wang S, Zhao S H, Shi Z W, Wu F Q, Zhao Z Y, Jiang L L, Watanabe K, Taniguchi T, Zettl A, Zhou C W, and Wang F 2020 *Nat. Mater.* **19** 986
[26] Kane C L, Mukhopadhyay R, and Lubensky T C 2002 *Phys. Rev. Lett.* **88** 036401
[27] Vishwanath A and Carpentier D 2001 *Phys. Rev. Lett.* **86** 676
[28] Roberts J A, Yu S J, Ho P H, Schoeche S, Falk A L, and Fan J A 2019 *Nano Lett.* **19** 3131
[29] Nefedov I S and Tretyakov S A 2011 *Photon. Nanostruct. – Fundam. Appl.* **9** 374
[30] Mikki S M and Kishk A A 2009 *IEEE Trans. Antennas Propag.* **57** 1412
[31] Polozkov R G, Senkevich N Y, Morina S, Kuzhir P, Portnoi M E, and Shelykh I A 2019 *Phys. Rev. B* **100** 235401
[32] Nefedov I S 2010 *Phys. Rev. B* **82** 155423
[33] Li H, Ying Z, Lyu B, Deng A, Wang L, Taniguchi T, Watanabe K, and Shi Z 2018 *Nano Lett.* **18** 8011
[34] Franck P, Baillargeat D, and Tay B K 2012 *IEEE Trans. Nanotechnol.* **11** 964
[35] Zhang Z, Chen Y, Shen P, Chen J, Wang S, Wang B, Ma S, Lyu B, Zhou X, Lou S, Wu Z, Xie Y, Zhang C, Wang L, Xu K, Li H, Wang G, Watanabe K, Taniguchi T, Qian D, Jia J, Liang Q, Wang X, Yang W, Zhang G, Jin C, Ouyang W, and Shi Z 2025 *Science* **387** 1310
[36] Liu K, Deslippe J, Xiao F, Capaz R B, Hong X, Aloni S, Zettl A, Wang W, Bai X, Louie S G, Wang E, and Wang F 2012 *Nat. Nanotech.* **7** 325
[37] Kane C, Balents L, and Fisher M P A 1997 *Phys. Rev. Lett.* **79** 5086
[38] Wang S, Wu F, Zhao S, Watanabe K, Taniguchi T, Zhou C, and Wang F 2019 *Nano Lett.* **19** 2360
[39] Clarke D G, Strong S P, and Anderson P W 1994 *Phys. Rev. Lett.* **72** 3218
[40] Neupert T, Chamon C, Mudry C, and Thomale R 2014 *Phys. Rev. B* **90** 205101
[41] Meng T 2020 *Eur. Phys. J. Spec. Top.* **229** 527
[42] Sondhi S L and Yang K 2001 *Phys. Rev. B* **63** 054430
[43] Teo J C Y and Kane C L 2014 *Phys. Rev. B* **89** 085101
[44] Slepyan G Y, Maksimenko S A, Lakhtakia A, Yevtushenko O, and Gusakov A V 1999 *Phys. Rev. B* **60** 17136
[45] Wilder J W G, Venema L C, Rinzler A G, Smalley R E, and Dekker C 1998 *Nature* **391** 59
[46] Garnett J C M and Larmor J 1904 *Philos. Trans. R. Soc. Lond. A* **203** 385
[47] Markel V A 2016 *J. Opt. Soc. Am. A.* **33** 1244